






Robust charge-density wave strengthened by electron correlations in monolayer 1T-TaSe₂ and 1T-NbSe₂

Yuki Nakata¹, Katsuaki Sugawara ^{1,2,3}, Ashish Chainani⁴, Hirofumi Oka ³, Changhua Bao⁵, Shaohua Zhou⁵, Pei-Yu Chuang⁴, Cheng-Maw Cheng ⁴, Tappei Kawakami¹, Yasuaki Saruta¹, Tomoteru Fukumura⁶, Shuyun Zhou ^{5,7}, Takashi Takahashi^{1,2,3} & Takafumi Sato ^{1,2,3}✉

Combination of low-dimensionality and electron correlation is vital for exotic quantum phenomena such as the Mott-insulating phase and high-temperature superconductivity. Transition-metal dichalcogenide (TMD) 1T-TaS₂ has evoked great interest owing to its unique nonmagnetic Mott-insulator nature coupled with a charge-density-wave (CDW). To functionalize such a complex phase, it is essential to enhance the CDW-Mott transition temperature $T_{\text{CDW-Mott}}$ whereas this was difficult for bulk TMDs with $T_{\text{CDW-Mott}} < 200$ K. Here we report a strong-coupling 2D CDW-Mott phase with a transition temperature onset of ~530 K in monolayer 1T-TaSe₂. Furthermore, the electron correlation derived lower Hubbard band survives under external perturbations such as carrier doping and photoexcitation, in contrast to the bulk counterpart. The enhanced Mott-Hubbard and CDW gaps for monolayer TaSe₂ compared to NbSe₂, originating in the lattice distortion assisted by strengthened correlations and disappearance of interlayer hopping, suggest stabilization of a likely nonmagnetic CDW-Mott insulator phase well above the room temperature. The present result lays the foundation for realizing monolayer CDW-Mott insulator based devices operating at room temperature.

¹Department of Physics, Graduate School of Science, Tohoku University, Sendai 980-8578, Japan. ²Center for Spintronics Research Network, Tohoku University, Sendai 980-8577, Japan. ³Advanced Institute for Materials Research (WPI-AIMR), Tohoku University, Sendai 980-8577, Japan. ⁴National Synchrotron Radiation Research Center, Hsinchu 30077, Taiwan ROC. ⁵State Key Laboratory of Low Dimensional Quantum Physics and Department of Physics, Tsinghua University, Beijing 100084, China. ⁶Department of Chemistry, Graduate School of Science, Tohoku University, Sendai 980-8578, Japan. ⁷Frontier Science Center for Quantum Information, Beijing 100084, China. ✉email: t-sato@arpes.phys.tohoku.ac.jp

The interplay among electron correlation, dimensionality, and appearance of various quantum phases is a long-standing issue in condensed-matter physics. The correlated electron system is characterized by strong Coulomb interactions among electrons and the resultant emergence of exotic physical properties, which are absent in the weakly interacting electron system. The most drastic consequence of electron correlation is the typical Mott–Hubbard transition^{1,2} that converts a half-filled paramagnetic metal (predicted by single-particle theory) into an antiferromagnetic insulator when the on-site Coulomb interaction U exceeds the bandwidth W (i.e., effective Coulomb interaction $U/W > 1$). A more unusual phase is the nonmagnetic Mott insulator and associated exotic quantum phases, as highlighted by the quantum-spin-liquid phase in 1T-TaS₂, a triangular lattice of two-dimensional (2D) Mott insulator with a CDW^{3,4}. In comparison, the destruction of antiferromagnetic order in doped copper oxides leads to emergence of high-temperature superconductivity that coexists with charge order^{5,6}.

To realize a Mott insulator, it is essential that the magnitude of U/W is above a critical value relevant to the structure and the electronic states of a material^{1,2}. In fact, for an optimally doped copper oxide, the large U (~ 3 eV)⁷ estimated for Cu-3d electrons compared with the relatively small bandwidth W (~ 0.4 eV)⁸ also satisfies the condition of $U/W \gg 1$. This suggests a direct relation between Mott physics and superconductivity (note that, in cuprates, the role of U is actually played by the charge-transfer gap of 1.4–2.0 eV⁹, but even in this case, the effective U/W (3.5–5.0) exceeds the critical value). However, the recent discovery of a Mott-insulator phase and associated superconductivity in tilted bilayer graphene^{10,11} demonstrated that even when U is considerably small (~ 30 meV), the band narrowing ($W \sim 20$ meV) introduced by the superstructure of moiré pattern can effectively convert a metallic state into a Mott-insulating one. This points to the importance of bandwidth control for materials with small U to trigger the Mott transition.

The layered transition-metal dichalcogenide (TMD) 1T-TaS₂ is believed to be a special example of a bandwidth-controlled Mott-transition material^{12,13} in the absence of magnetic order. Bulk 1T-TaS₂ undergoes a Mott transition accompanying a commensurate charge-density wave (CDW) characterized by the star-of-David cluster (Fig. 1a) with a $\sqrt{13} \times \sqrt{13}$ periodicity (Fig. 1b), at $T_{\text{CDW-Mott}} \sim 200$ K. It is noted that twelve Ta atoms located at the corners of a cluster are slightly displaced from the original position toward the central Ta atom (Fig. 1a). 1T-TaS₂ satisfies the half-filling condition necessary for realizing a Mott-insulator phase, since 12 electrons at the displaced 12 Ta atoms form the fully occupied 6 bands and the remaining electron at the central Ta atom forms a half-filled metallic band^{14,15}. Although the U of Ta 5d electrons is relatively small (~ 0.7 eV)¹⁶, 1T-TaS₂ undergoes the Mott transition when the half-filled band is narrowed to the scale of U due to the band folding associated with the CDW^{12,13} in a similar manner to tilted bilayer graphene. More interestingly, it was shown that while it has a charge gap of ~ 0.3 eV, it shows gapless quantum-spin-liquid dynamics and no long-range magnetic order down to 70 mK¹⁷. Recently, the exploration for Mott phases coexisting with CDW was extended to the atomic-layer limit in TMDs as in graphite (graphene), with the possible emergence of exotic quantum phenomena in the pure 2D limit^{18–20}. However, the nature of a pure 2D CDW–Mott phase, such as its robustness, possibility for magnetism, and differences if any, compared with the 3D bulk case, has been scarcely explored experimentally. In particular, the essential issue regarding the interplay between the Mott phase and dimensionality is yet to be clarified.

In this work, we address all the above key issues by performing a comprehensive angle-resolved photoemission spectroscopy

(ARPES) study on epitaxially grown monolayer 1T-TaSe₂ and 1T-NbSe₂, and demonstrate the robust CDW–Mott phase under external perturbations such as heating and electron doping.

Results and discussion

Characterization of TaSe₂. First, we discuss the electronic structure of monolayer 1T-TaSe₂ whose monolayer nature was confirmed by our scanning tunneling microscopy (STM) measurement (Supplementary note 1). Figure 1c displays the 3D ARPES intensity plotted as a function of 2D wave vector (k_x and k_y) and binding energy E_B measured at $T = 40$ K. One can clearly recognize a nearly flat band at $E_B \sim 0.3$ eV and dispersive holelike bands topped at the Γ point, which are ascribed to the Ta 5d and Se 4p bands, respectively¹⁸. The topmost Ta 5d band does not cross the Fermi level (E_F) and exhibits an insulating gap of ~ 0.3 eV below E_F at the Γ point. This gap is not assigned to a band gap, a substrate-induced gap, or a conventional CDW gap (Supplementary note 2), but to a Mott–Hubbard gap. This Mott gap is associated with the enhancement of U/W caused by the hybridization of backfolded bands and the resultant band narrowing due to the $\sqrt{13} \times \sqrt{13}$ commensurate CDW (Fig. 1b), as in bulk nonmagnetic 1T-TaS₂^{12,13} and a surface layer of bulk 1T-TaSe₂^{21,22} as can be suggested from the overall similarity of experimental band dispersion (Supplementary Fig. S2). The gap size below E_F , called here Δ_{Mott} , roughly corresponds to a half of the full Mott-gap size $2\Delta_{\text{Mott}}$ because E_F is nearly located at the midpoint between the lower Hubbard band (LHB) and the upper Hubbard band (UHB) as suggested from the comparison of ARPES and tunneling spectroscopy data^{20,23,24} (Supplementary note 3). As shown in Fig. 1c, a signature of the CDW is clearly seen as an apparent hybridization-gap discontinuity^{21,22} in the band dispersion at $k \sim 2/3$ ΓM (red dashed line, see Fig. 1c). It is important to note that we could selectively fabricate a pure 1T-TaSe₂ phase (and also 1T-NbSe₂ phase, discussed later) with ease by controlling the substrate temperature¹⁸. This enables observation of a clear hybridization-gap discontinuity in our data as compared with a recent study, where admixture from the 1H-TaSe₂ phase made it difficult to see the discontinuity²⁰. The STM image in Fig. 1d obtained in a spatial region of 8×8 nm² on a monolayer TaSe₂ island signifies a clear periodic modulation associated with the formation of CDW containing the hexagonal lattice of star-of-David clusters. We have confirmed that this lattice has a periodicity of $\sqrt{13} \times \sqrt{13}R13.9^\circ$ expected for the formation of star-of-David lattice, as well visible as superspots in the Fourier transform image shown in Fig. 1e, in agreement with the previous STM study of monolayer 1T-TaSe₂²⁰.

The Ta 4f core-level spectroscopy (Fig. 1f) signifies that the Ta 4f_{5/2} and 4f_{7/2} spin-orbit satellite peaks split into two subpeaks, as is clearly visible in the energy-distribution curve (EDC) at $T = 40$ K. Since the additional splitting of Ta-4f peak is attributed to the different electron density at each Ta site^{25,26} and/or the change in the chemical bonding of Ta atoms due to the formation of the star-of-David clusters, the core-level spectrum is consistent with our STM data that support the formation of the star-of-David clusters. On elevating temperature, we found that the lower-binding-energy subpeak of both the Ta4f_{5/2} and 4f_{7/2} components is gradually weakened, but the shoulder feature still remains even at $T = 400$ K. This implies that the Mott phase survives much above the room temperature. We will come back to this point later.

Temperature dependence of the Mott gap. The formation of CDW is further corroborated by the appearance of a LHB in the ARPES intensity at $T = 300$ K (Fig. 2b), similarly to the case at $T = 40$ K (Fig. 2a), because the Mott gap cannot be formed

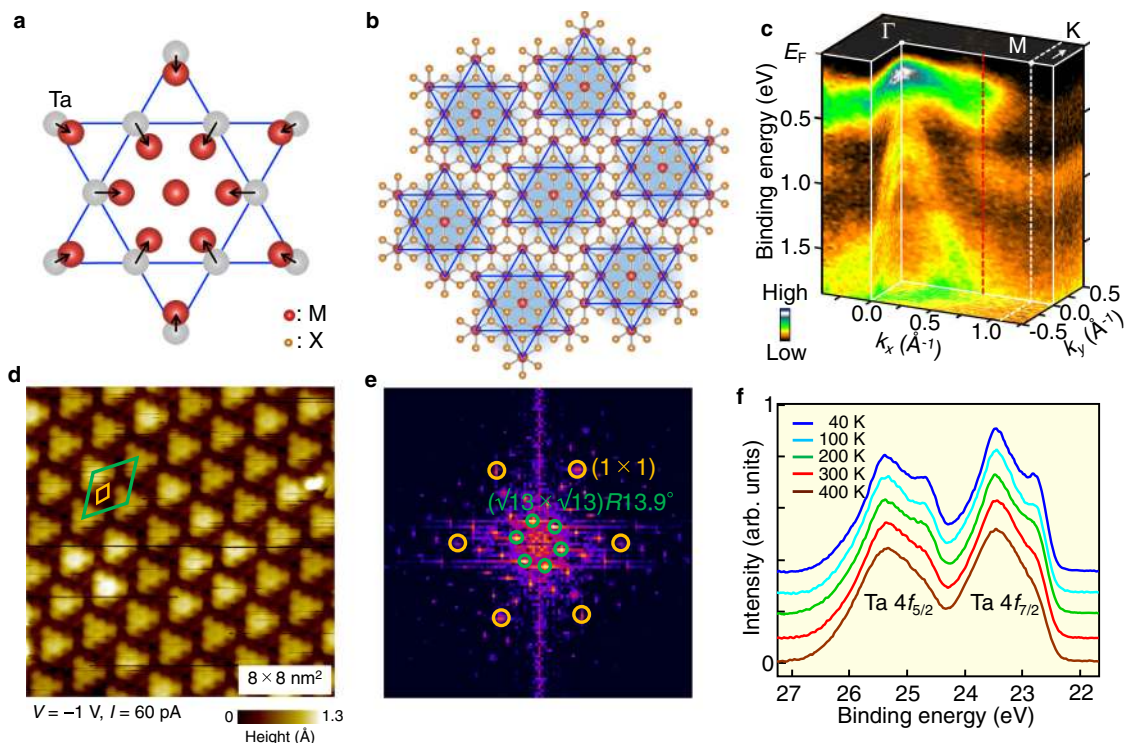


Fig. 1 Schematics of star-of-David clusters and core-level photoemission spectrum of monolayer 1T-TaSe₂. **a** Schematics of the displacement of Ta atoms in the star-of-David cluster. M and X represent transition-metal and chalcogen atoms, respectively. **b** Schematics of crystal structure for monolayer 1T-TaSe₂ and star-of-David clusters with the $\sqrt{13} \times \sqrt{13}$ periodicity. **c** 3D ARPES-intensity plot as a function of 2D wave vector (k_x and k_y) and E_B for monolayer 1T-TaSe₂ measured at $T = 40$ K with the He-I α line ($h\nu = 21.218$ eV). Hybridization gap ($k_x - 2/3 \Gamma M$) is indicated by red dashed line. **d** STM image in a surface area of 8×8 nm² for monolayer 1T-TaSe₂ on bilayer graphene measured at $T = 4.8$ K. **e** Fourier transform image of **d**. **f** Temperature dependence of EDC around the Ta-4f core level measured with $h\nu = 260$ eV for monolayer 1T-TaSe₂.

without the CDW^{12,13}. Intriguingly, the LHB survives even upto $T = 450$ K (the highest temperature in our experimental setup, see Fig. 2c), whereas the overall spectral feature becomes less clear. Such spectral feature at $T = 450$ K cannot be explained in terms of the absence of Mott gap and the persistence of CDW gap because of the following reason. In bulk TaSe₂²⁷, the LHB essentially vanishes at room temperature and a large metallic spectral weight emerges at E_F , in contrast to the low-temperature (70–220 K) data that display a peak associated with the LHB. Our ARPES data for monolayer 1T-TaSe₂ at room temperature resemble that of bulk TaSe₂ at low temperature (Fig. 2d), suggestive of the persistence of a Mott gap at $T = 450$ K (Supplementary note 4). The robustness of Mott gap is also seen from the detailed temperature dependence of EDC at the Γ point in Fig. 2d. This is in stark contrast to bulk 1T-TaS₂ where a metallic Fermi edge is recovered at $T = 300$ K. Also, this is distinct from bulk 1T-TaSe₂ that shows a clear Fermi-edge cutoff even at $T = 30$ K (Fig. 2d) and hence, we compared the T -dependent behavior of the clear gap observed in monolayer 1T-TaSe₂ with bulk 1T-TaS₂.

To discuss more quantitatively the gap behavior, we plot the binding energy of the leading-edge midpoint of the EDC, Δ_{LEM} , as a function of temperature for monolayer 1T-TaSe₂, and compare it with that for bulk 1T-TaS₂. We expect Δ_{LEM} to be directly related with the transport gap in the monolayer instead of the spectroscopic gap Δ_{Mott} (for the difference between Δ_{LEM} and Δ_{Mott} , see Supplementary note 5). As one can see from the Δ_{LEM}^2 vs T plot in Fig. 2e, Δ_{LEM}^2 for monolayer 1T-TaSe₂ shows a nearly linear behavior as a function of T near $T_{CDW-Mott}$ and exhibits a finite value even at 450 K. This nearly linear behavior is also seen in bulk 1T-TaS₂ as shown in Fig. 2e, and was also reported for

bulk and monolayer 1T-TiSe₂ recently²⁸. The T dependence of Δ_{LEM} is well reproduced by a semiphenomenological BCS gap equation based on the mean-field approximation (blue solid curve) expressed as $\Delta_{LEM}(T) = \Delta_{LEM} (T_{CDW-Mott})^2 \propto \tanh^2(A\sqrt{(T_{CDW-Mott}/T) - 1})$, where Δ_{LEM} , $T_{CDW-Mott}$ and A are the binding energy of the leading-edge midpoint, the CDW-Mott transition temperature, and the proportional constant, respectively²⁸, which was recently used to characterize bulk and monolayer 1T-TiSe₂ (note that the observed temperature dependence of EDC can hardly be explained with the thermal broadening; for details, see Supplementary note 4). From the numerical fittings, the transition temperature was estimated to be $T_{CDW-Mott} \sim 530$ K for monolayer 1T-TaSe₂, and this is much higher than that obtained for bulk 1T-TaS₂ (<200 K; red circles and curves). The present results suggest that the CDW-Mott-transition temperature $T_{CDW-Mott}$ of monolayer TaSe₂ is very high, being drastically higher than that of bulk TaS₂ ($T_{CDW-Mott} \sim 200$ K)¹² and a surface layer of bulk TaSe₂ ($T_{CDW-Mott} \sim 260$ K)^{27,29} (note that a consensus has not been reached for the exact $T_{CDW-Mott}$ value at the surface of TaSe₂; Supplementary note 6 and Fig. S5). In contrast, the increase in T_{CDW} of 1T-TiSe₂ in going from bulk ($T_{CDW} \sim 200$ K) to monolayer ($T_{CDW} \sim 235$ K) was small^{28,30}. If we consider Δ_{LEM} to be a measure of half the transport gap (since E_F lies in the middle of the gap, as discussed earlier), $2\Delta_{LEM}(T=0)/k_B T_{CDW-Mott} \sim 12$, which is significantly larger than the weak-coupling result of ~ 3.52 . Thus, monolayer 1T-TaSe₂ can be classified as a strongly coupled CDW-Mott phase. It is noted that our time-resolved ARPES experiment suggests that the LHB of monolayer TaSe₂ survived after photoexcitation even when we adopted the maximum pump fluence above which monolayer samples were damaged

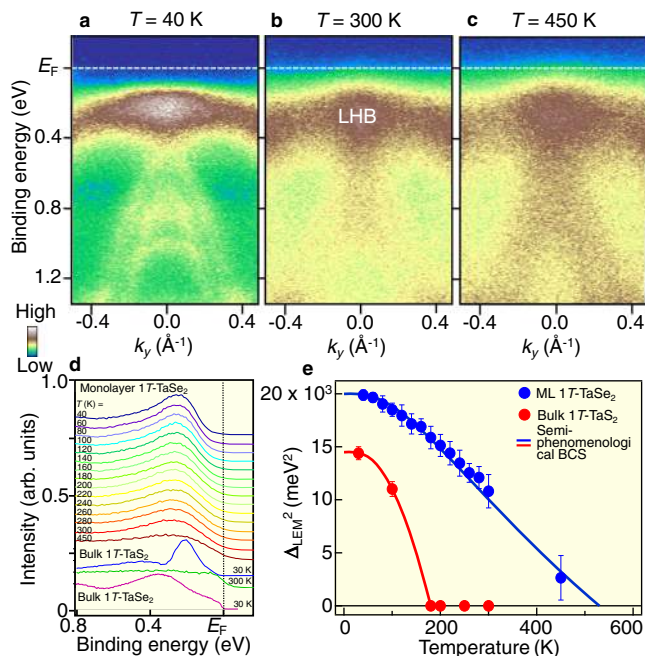


Fig. 2 CDW-Mott phase of monolayer 1T-TaSe₂ robust against temperature variation. **a–c** Near- E_F ARPES intensity along the Γ K cut measured at $T = 40, 300,$ and 450 K, respectively. **d** Temperature dependence of EDC at the Γ point. EDC for bulk 1T-TaSe₂ ($T = 30$ and 300 K) and bulk 1T-TaSe₂ ($T = 30$ K) is also shown as a reference. **e** Squared leading-edge midpoint Δ_{LEM}^2 at the Γ point plotted against T for monolayer 1T-TaSe₂ (blue circles), together with the numerical fitting results with the semi-phenomenological (blue solid curve) BCS gap functions. Δ_{LEM}^2 and fitting results are also plotted for bulk 1T-TaSe₂ (red). We have obtained $\{T_{CDW-Mott}, A\} = \{530 \text{ K}, 1.01\}$ and $\{180 \text{ K}, 1.50\}$ for monolayer 1T-TaSe₂ and bulk 1T-TaSe₂, respectively. Error bars in **e** reflect the uncertainties originating from the energy resolution and the standard deviation in the peak positions of EDCs.

(this maximum pump fluence is lower than that in bulk TaSe₂,^{31–36} for details, see Supplementary note 7 and Fig. S6).

Carrier doping effect to the Mott gap. Next, we show the robustness of the LHB against carrier doping. Figures 3a–c show the evolution of ARPES intensity as a function of potassium (K) coverage d_K [0 (pristine), 3.2 and 6.4×10^{13} atoms/cm²] and the corresponding second-derivative intensity plots (d–f) (for details of the d_K estimation, see Methods section). Upon K deposition of $d_K = 3.2 \times 10^{13}$ atoms/cm², which corresponds to $\sim 50\%$ of the star-of-David density (Fig. 3b), the band structure is shifted downward as a whole with respect to pristine TaSe₂ (Fig. 3a) due to the electron doping from K atoms. This suggests that the K deposition dopes electron carriers into a whole monolayer film, as in the case of other monolayer TMD films such as TiSe₂ where K deposition causes an overall downward shift of the band structure and disappearance of CDW³⁷. On further depositing K atoms (Fig. 3c), the spectral feature becomes significantly broad due to the strong electron scattering by the K-induced disorder, whereas a broad hump originating from the LHB is still seen at $E_B \sim 0.6$ eV in the EDC in Fig. 3g. The LHB and its systematic downward shift are better visualized in the second-derivative-intensity plots in Fig. 3d–f. A careful look at the intensity for $d_K = 6.4 \times 10^{13}$ atoms/cm² (Fig. 3f) reveals a bright intensity in the vicinity of E_F , which originates from a finite Fermi-edge cutoff, as also seen in the EDC (green curve) in Fig. 3g.

To discuss the spectral evolution upon K dosing in more detail, we have analyzed the spectral weight at E_F relative to that of LHB, I_{EF}/I_{LHB} , as a function of K coverage d_K . As shown in Fig. 3h, the I_{EF}/I_{LHB} value (red circles) does not exhibit a monotonic behavior as a function of d_K , showing a minimum at $d_K = 3.2 \times 10^{13}$ atoms/cm². The nonzero value for $d_K = 0$ atoms/cm² may be associated with the tail of LHB extending toward E_F , as also seen in the EDC (Fig. 3g). We found that the I_{EF}/I_{LHB} value in monolayer for both $d_K = 3.2$ and 6.4×10^{13} atoms/cm² is larger than that of the CDW–Mott insulator phase ($T = 30$ K) in bulk TaSe₂ (blue square), implying a possible metallic behavior. We have confirmed that such a difference between monolayer and bulk is not associated with the difference in the experimental conditions. This can be seen from Fig. 3h where I_{EF}/I_{LHB} at $T = 300$ K for monolayer 1T-TaSe₂ ($d_K = 0$) obtained with He lamp (green circle) and synchrotron radiation (red circle) will coincide with each other within our experimental uncertainty.

A simple explanation to account for the observed metallic component may be electron occupation of the UHB. Since the energy position of LHB shifts from 0.28 eV to 0.75 eV with K deposition (Fig. 3g), one would expect the UHB to appear below E_F in the $d_K = 6.4 \times 10^{13}$ atoms/cm² sample since the full Mott gap is estimated to be 0.5 eV (Supplementary note 3). However, we found no evidence for the prominent peak from the UHB. This is reasonable because the high Coulomb cost U to populate an electron to the UHB does not guarantee the rigid-band-like electron doping. As an alternative possibility, a metallic K component due to the high density of K atoms (which produces an angle-integrated-type background with a weak Fermi-edge cutoff in EDC) or in-gap states (with suppressed quasiparticle intensity and reduced lifetime) could be conceived. The latter possibility is expected from the Hubbard model for the doped Mott insulator and was observed in spectroscopic studies of cuprates³⁸.

As shown in Fig. 3h, the I_{EF}/I_{LHB} value in the monolayer sample of $d_K = 6.4 \times 10^{13}$ atoms/cm² is much smaller than that in the bulk counterpart with the fully melted CDW–Mott state at $T = 300$ K (yellow square). This implies that the framework of LHB itself is still maintained in the monolayer even when the system likely becomes metallic upon electron doping, in contrast to the bulk counterpart where even a small amount of electron doping breaks the LHB and leads to the occurrence of superconductivity^{39–42}. In particular, doping electrons by substitution of magnetic Fe ions in 1T-Fe_xTa_{1-x}Se₂ was shown to result in a dispersive electron band accompanied by a destruction of the LHB even with 1% Fe substitution^{40,41}. A plausible mechanism of such fragileness in bulk is associated with the Fermi-surface nesting condition that is sensitive to the carrier doping, and has been discussed as a primary cause of incommensurate CDW and the resultant Mott phase in bulk 1T-TaSe₂^{43,44}. In this regard, the monolayer data are puzzling and surprising because the LHB still survives even when the nesting condition is modified by the electron doping. In any case, the survival of LHB suggests that the electron correlation is still strong even in the doped monolayer sample.

A recent generalized-gradient approximation band-structure calculation with on-site Coulomb interaction (GGA + U) for isoelectronic 1T-NbSe₂⁴⁵ has reproduced the LHB and Mott gap, consistent with the ARPES data. It is noted though, while the GGA + U study and a very recent DFT (density-function-theory) calculation with GGA on monolayer 1T-TaSe₂⁴⁶ suggested a spin-1/2 ferromagnetic Mott-insulator phase, our experimental attempt to detect possible ferromagnetism was not successful [since the detection of ferromagnetism by macroscopic magnetization measurement is difficult for monolayer samples, we carried out a very primitive experiment by just putting a strong

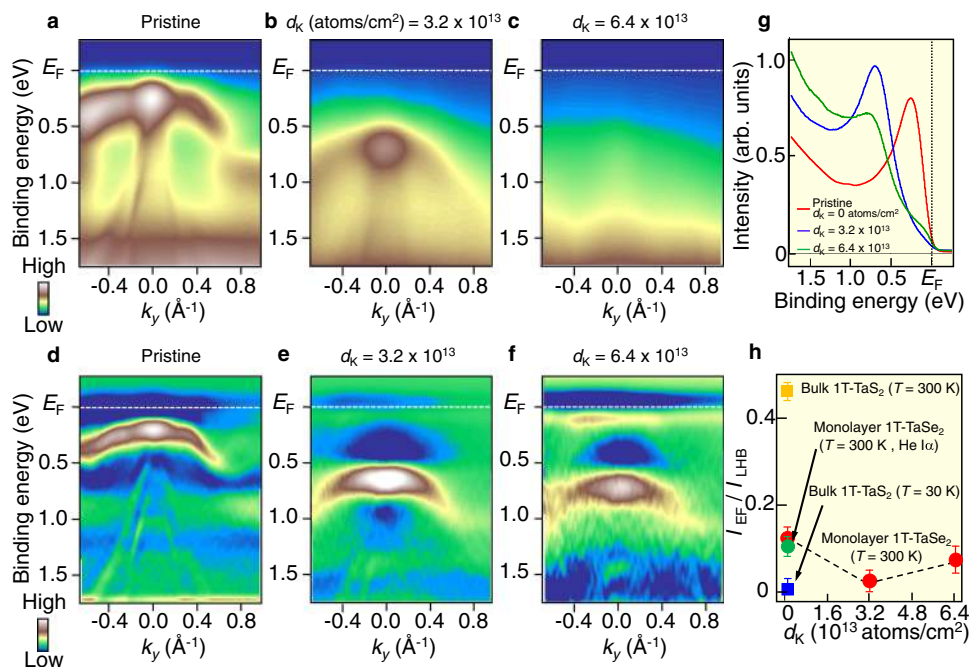


Fig. 3 CDW-Mott insulator phase in monolayer 1T-TaSe₂ robust against electron doping. **a-c** K-deposition dependence of ARPES intensity along the Γ K cut for monolayer 1T-TaSe₂ [potassium coverage $d_K = 0$ (pristine), 3.2×10^{13} , and 6.4×10^{13} atoms/cm², respectively], measured at $T = 300$ K with $h\nu = 51$ eV. **d-f** Same as **a-c**, but obtained by taking the second derivative of EDCs. **g** EDCs at the Γ point for each d_K . **h** Plots of intensity at E_F with respect to that at LHB, I_{EF}/I_{LHB} , as a function of d_K , estimated from the EDCs in **g**. The values for bulk TaSe₂ measured at $T = 30$ and 300 K are also plotted. Error bars reflect the uncertainties originating from the energy resolution and statistics of data. Asymmetry in the intensity profile in **a** and **b** is associated with the inequivalent photoelectron matrix-element effect between positive and negative k_y 's (Supplementary note 8 and Fig. S7).

Nd magnet (magnetic field ~ 500 mT) on top of a film to detect possible attractive force]. A good agreement of the overall band structure in the Mott-insulator phase between monolayer TaSe₂ and bulk nonmagnetic 1T-TaSe₂⁴¹ may support the nonmagnetic ground state of monolayer TaSe₂, although this point needs to be verified in future, e.g., by X-ray magnetic circular dichroism measurement.

Comparison between TaSe₂ and NbSe₂. Now that the survival of LHB in various conditions is established for monolayer TaSe₂, next, we explore the CDW-Mott phase in a cousin material, monolayer 1T-NbSe₂. One can immediately recognize in the ARPES intensity along the Γ K cut in Fig. 4a that the LHB is well seen at $T = 40$ K in monolayer NbSe₂. The LHB survives even at $T = 450$ K (Fig. 4b), as is also visible in the EDC at the Γ point in Fig. 4c. A side-by-side comparison of the valence-band ARPES intensity along the Γ M cut between monolayer TaSe₂ and NbSe₂ in Fig. 4d, e reveals several common features, such as a nearly flat LHB, dispersive hole-like Se-4p bands, and a discontinuity of band dispersion at $k_x \sim 2/3$ Γ M caused by the hybridization-gap opening due to the CDW. These results demonstrate that the robust Mott-insulator phase coexisting with CDW upon heating is a common characteristic for monolayer TaSe₂ and NbSe₂.

In the following, we discuss why the LHB in monolayer TaSe₂ and NbSe₂ is robust unlike in the bulk counterpart. Since one of the key parameters to trigger a CDW-Mott transition is the effective Coulomb interaction U/W , it is important to discuss the independent roles of how U and W are independently affected on going from the bulk 3D structure to the monolayer 2D case. The effective on-site Coulomb correlation energy can be described by the equation $U = E_I - E_A - E_{Pol}$ where, E_I is the ionization energy, E_A is the electron affinity, and E_{Pol} is the polarization energy that arises from screening due to any electronic perturbation such as removing or adding an electron. This screening causes a strong

reduction of U compared with the bare Coulomb interaction $U_{bare} (= E_I - E_A)$. For example, based on a one-band Hubbard model, U for the Cu site gets reduced to ~ 4 eV in La₂CuO₄ compared with $U_{bare} \sim 20$ eV for Cu atom⁴⁷. For 4d and 5d transition metals, U is expected to be still lower. For 1T-TaSe₂, 1T-TaSe₂, and 1T-NbSe₂, typical values of U reported in the literature range from $\sim 0.4/0.7$ eV (in the GW approximation/DFT-DMFT approximation^{16,48}) to $\sim 2.0/2.8$ eV (in GGA + U)^{20,49,50}. Considering the role of screening in monolayer compared to the bulk case, while the intralayer E_{Pol} is expected to show negligible changes in the monolayer case, the interlayer E_{Pol} would be suppressed as there are no other layers and the interaction with the substrate is weak, resulting in an effective increase in U compared with the bulk.

Similarly, since there is no out-of-plane or interlayer hopping in the monolayer, i.e., the intrinsic bulk interlayer bandwidth W_{out} is absent, the net effective bandwidth W will get reduced. It was suggested from the first-principles band-structure calculations that, although the in-plane bandwidth W_{in} becomes significantly small (~ 0.08 eV⁵¹) due to the band reconstruction associated with CDW, the out-of-plane bandwidth W_{out} (~ 0.54 eV⁵¹) does not suffer from a strong band-narrowing effect because of the in-plane nature of CDW. In this case, the dominant channel to determine the total W is the interlayer hopping (Fig. 5b) (note that the inter- and intralayer hopping channels do not contribute in an additive way to the bandwidth, but one can still discuss which plays a dominant role). It is thus inferred that the U/W value in the bulk is largely governed by the interlayer hopping and the bulk is located on the verge of the CDW-Mott transition ($U/W \sim 1.3$;⁴⁸ note that U is ~ 0.7 eV in TaSe₂¹⁶). On the other hand, in monolayer, the interlayer hopping is intrinsically absent (Fig. 5b) and the net W is simply associated with the intralayer hopping. Thus, both the increase in U and decrease in W are expected to positively work together to

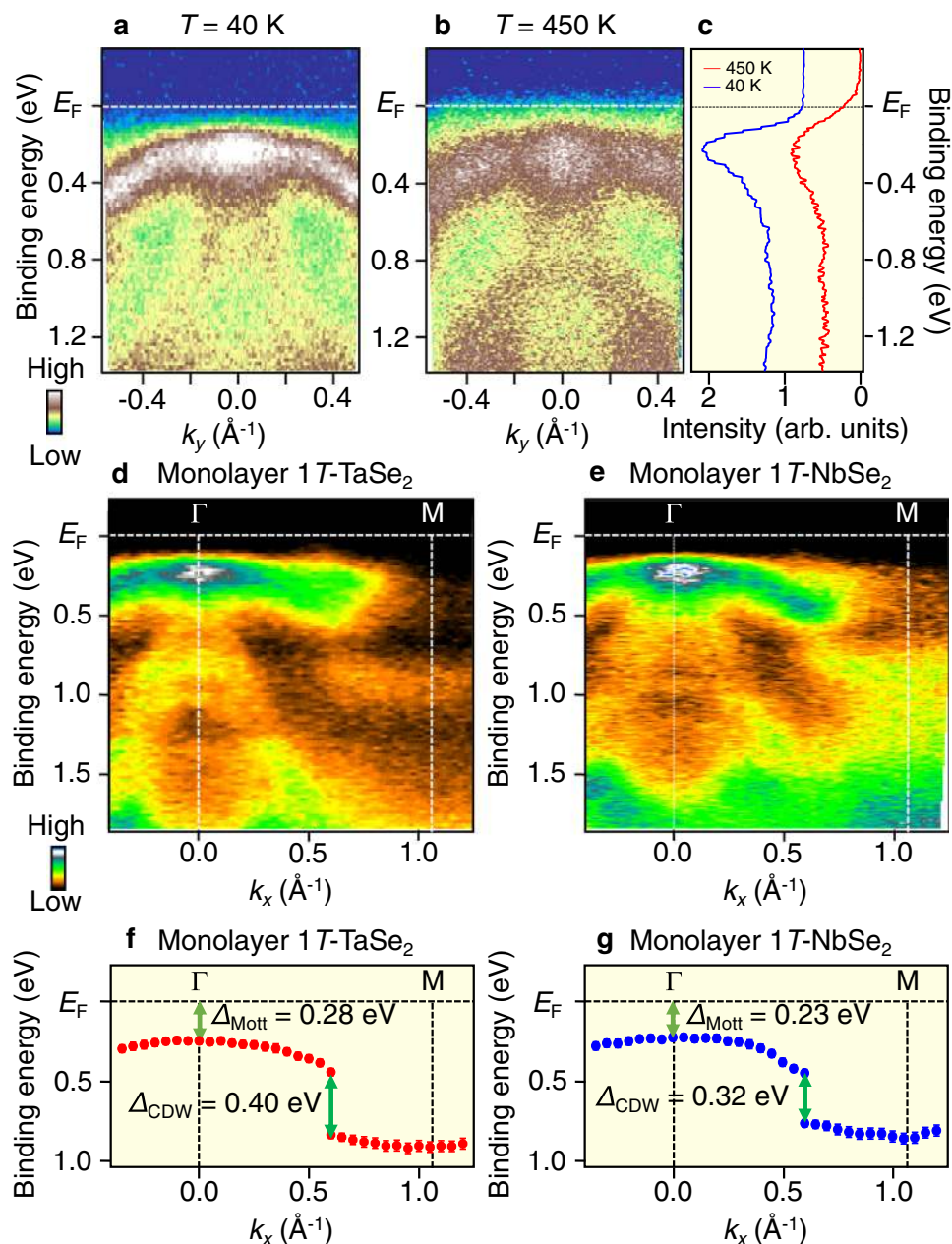


Fig. 4 Comparison of the CDW-Mott phase between monolayer NbSe₂ and TaSe₂. **a, b** ARPES intensity of monolayer 1T-NbSe₂ at $T = 40$ and 450 K, respectively, measured along the ΓK cut. **c** EDCs at the Γ point at $T = 40$ and 450 K. **d, e** Valence-band ARPES intensity along the ΓM cut for monolayer NbSe₂ and TaSe₂, respectively. **f, g** Experimental band dispersion extracted by tracing the peak position in EDCs for monolayer TaSe₂ and NbSe₂, respectively, highlighting the quantitative difference in the magnitude of the Mott-Hubbard gap (Δ_{Mott}) and the hybridization gap associated with CDW (Δ_{CDW}). Error bars in **e** reflect the uncertainties originating from the energy resolution and the standard deviation in the peak positions of EDCs.

efficiently increase U/W , leading to the robust CDW-Mott phase far above bulk T_{Mott} . We remark here that it is difficult to experimentally determine W by simply tracing the continuously dispersing bands in the experiment, because such bands are composed of multiple subbands reconstructed by the CDW and the intensity of bands is often suppressed in the region away from the original unfolded band³³. The Mott transition is associated only with a half-filled subband crossing E_F , which has a narrow in-plane bandwidth W_{in} ³³, although previous ARPES studies above T_{Mott} on bulk TaS₂ (e.g.,^{21,26,27,41}) were unable to resolve this band, probably because of the smearing of fine-band structure by, e.g., thermal broadening.

A comparison of characteristic energy scales between monolayer TaSe₂ and NbSe₂ reveals an intriguing aspect of the

CDW-Mott phase in the two systems (Fig. 4d and e). As shown in the ARPES-derived band dispersions in Fig. 4f and g, a half of the full Mott gap, Δ_{Mott} , in TaSe₂ (0.28 ± 0.02 eV) is slightly larger than that in NbSe₂ (0.23 ± 0.02 eV). Also, the hybridization gap Δ_{CDW} in TaSe₂ (0.40 ± 0.03 eV) is larger than that in NbSe₂ (0.32 ± 0.03 eV). According to the general trend of U in $3d-4d-5d$ electron systems, U for the Nb- $4d$ orbital is expected to be larger than that for the Ta- $5d$ orbital. Band-structure calculations suggested that the in-plane bandwidth of Nb $4d$ band in the normal state of monolayer NbSe₂ (~ 2.2 eV)⁴⁹ is smaller than that in monolayer TaSe₂ (~ 2.7 eV)⁵². It is expected from a simple band-folding picture that the bandwidth in the CDW phase W_{in} is also smaller in NbSe₂. Although this argument suggests a larger U/W and a resultant more stable CDW-Mott phase in NbSe₂

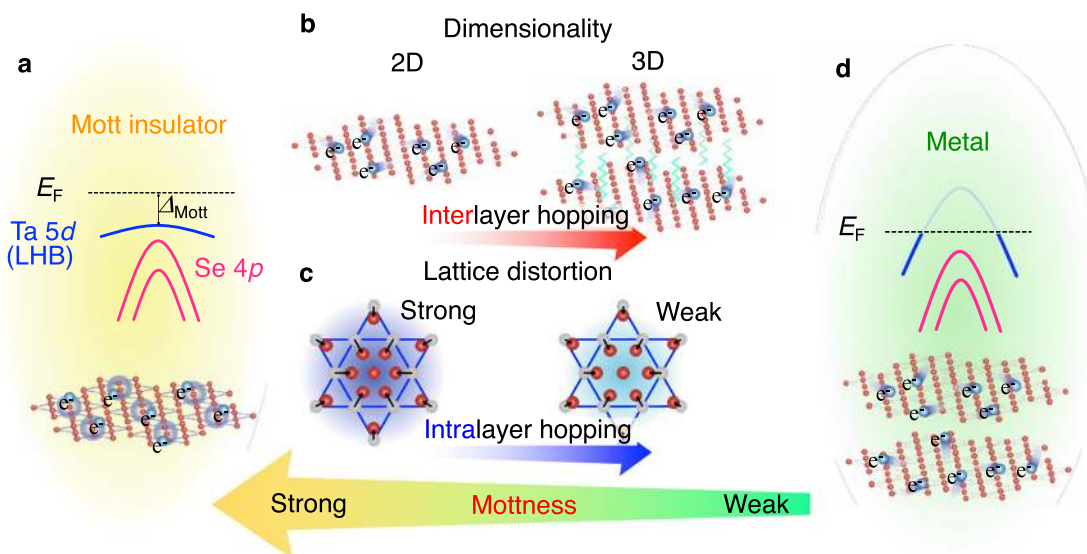


Fig. 5 Realization of 2D CDW-Mott insulator phase assisted by strong lattice distortion. **a** Schematics of (top) the band dispersion and (bottom) the star-of-David clusters in the robust CDW-Mott phase in monolayer TaSe₂. **b** Illustration to compare the interlayer hopping in the crystal in 2D and 3D systems. **c** Illustration of strong vs weak lattice distortion in the star-of-David cluster and its relationship with the intralayer hopping in the CDW phase. **d** Schematics of (top) the normal-state band dispersion and (bottom) the bulk crystal structure without CDW formation.

than in TaSe₂, the observed smaller Δ_{Mott} (0.23 eV) in NbSe₂ (this also implies lower T_{Mott}) apparently contradicts with the above simple argument. This discrepancy may be reconciled by taking into account the observed larger Δ_{CDW} (0.40 eV) in TaSe₂, which suggests a smaller intralayer hopping and as a result a larger U/W compared with NbSe₂ (note that while the bandwidth of LHB is estimated to be 0.19 and 0.21 eV for TaSe₂ and NbSe₂, respectively, these values cannot be regarded as W and one needs to know the original bare W without any influence from the Mott gap). This suggests that the lattice displacement in the star-of-David cluster is stronger in monolayer TaSe₂ (Fig. 5c; left), which is also inferred from the stronger metallic-bonding character of Ta than that of Nb. The stronger periodic lattice distortion due to the CDW in TaSe₂ is also supported by the observation of more pronounced hybridization-gap discontinuity around $k \sim 2/3 \Gamma\text{M}$ in TaSe₂, as seen from the stronger intensity suppression at $E_{\text{B}} \sim 0.6$ eV in Fig. 4d than that in Fig. 4e (note that some other experiments must be carried out to firmly establish the stronger CDW in TaSe₂). It is also noted that Δ_{CDW} of monolayer TaSe₂ (0.40 eV) is slightly larger than that of bulk TaSe₂ (0.37 eV);²² this suggests a stronger lattice distortion in monolayer systems, consistent with GGA + U calculations discussed above⁴⁵. All these arguments suggest that the robust CDW-Mott insulator phase of monolayer TaSe₂ and NbSe₂ (Fig. 5a) is caused by the disappearance of interlayer hopping assisted by a strong lattice distortion. In other words, the robust CDW in monolayer TaSe₂ and NbSe₂ is derived from a combination of electron correlations, a strong lattice distortion, and the absence of interlayer hopping. It is emphasized that such properties are all linked to the electron hopping (or electron kinetic energy) of the system (Fig. 5b and c), and the controllability of the Mottness (i.e., strength of the Mott phase) lies on how to effectively manipulate both inter- and intralayer hopping (Fig. 5a–d).

The present study has established an effective means to stabilize the CDW-Mott phase in terms of band engineering. Also, the discovery of the robust CDW-Mott phase far above the room temperature is useful for developing practical CDW-Mott insulator-based ultrathin nanoelectronic devices. It would be very interesting to explore the superconductivity in a metallic state near the Mott phase.

Methods

Sample preparation. Monolayer 1T-TaSe₂ and 1T-NbSe₂ films were grown on bilayer graphene/6H-SiC by using molecular-beam-epitaxy (MBE) method in an ultrahigh vacuum (UHV) of 3×10^{-10} Torr. As for the monolayer NbSe₂ film, we have adopted the same procedure to grow monolayer 1T-NbSe₂ established in our previous studies where the 1T structure, $\sqrt{13} \times \sqrt{13}$ lattice reconstruction, and its monolayer nature were already clarified^{19,53}. To fabricate a monolayer TaSe₂ film, we have also followed the fabrication method established by ourselves¹⁸. Specifically, bilayer graphene was prepared by annealing an *n*-type Si-rich 6H-SiC(0001) single-crystal wafer, with resistive heating at 1100 °C in ultrahigh vacuum better than 1×10^{-10} Torr for 30 min. A monolayer TaSe₂ (NbSe₂) film was grown by evaporating Ta (Nb) on the bilayer graphene substrate kept at 560 °C (580 °C) under a Se atmosphere^{18,19}. The as-grown film was subsequently annealed at 400 °C for 30 min. The growth process was monitored by reflection high-energy diffraction (RHEED). The film thickness was estimated by a quartz-oscillator thickness meter, scanning tunneling microscopy (STM), and atomic force microscopy (AFM). Based on our experience of fabricating various monolayer TMD films such as NbSe₂, VTe₂, VSe₂, and TiSe₂^{18,19,54,55}, a monolayer film is formed immediately after the disappearance of buffer-layer-originated $6\sqrt{3} \times 6\sqrt{3}$ RHEED pattern upon coevaporation of transition-metal and chalcogen atoms. We have judged the thickness of 1T-TaSe₂ and NbSe₂ films by monitoring this disappearance in the RHEED pattern. After the fabrication by the MBE method, the films were transferred to the ARPES-measurement chamber without breaking the vacuum. We have calibrated the deposition rate of K atoms by calculating the volume of π -band Fermi surface at the K point in bilayer graphene on SiC with keeping the same evaporation rate as that in the case of monolayer TaSe₂, and it is estimated to be 1.6×10^{13} atoms/cm²/min. We have deposited K atoms for 2 and 4 min, that corresponds to the K coverage d_{K} of 3.2 and 6.4×10^{13} atoms/cm², i.e., ~ 50 and $\sim 100\%$ of the star-of-David density, respectively. Thus, the amount of K dosing with respect to the star-of-David density is sufficient to achieve a sizable electron doping into monolayer 1T-TaSe₂.

ARPES and STM measurements. ARPES measurements were carried out using an MBS-A1 electron-energy analyzer with a high-flux helium-discharge lamp and a toroidal grating monochromator at Tohoku University and an Omicron-Scienta R4000 electron-energy analyzer with synchrotron radiation at Taiwan Light Source (TLS), National Synchrotron Radiation Research Center (NSRRC). The energy and angular resolutions were set to be 12.5–40 meV and 0.2°, respectively. Core-level photoemission-spectroscopy measurement was performed at BL28A with micro-focused beam spot in Photon Factory. Time-resolved ARPES measurements were carried out at Tsinghua University using an Omicron-Scienta DA30-L-8000 electron-energy analyzer and a Ti:sapphire oscillator that produces femtosecond pulses from 700 to 980 nm at 76 MHz repetition rate with pulse duration of ~ 130 fs. The time resolution was 480 fs when the probe photon energy was set to 6.2 eV⁵⁶. The infrared laser was frequency-quadrupled using BBO and KBBF crystals to produce an ultraviolet probe light from 177.5 to 230 nm. The beam sizes of pump and probe beam were set to $\sim 45 \mu\text{m}$ and $\sim 15 \mu\text{m}$ (full width at half maximum), respectively. The wavelengths of pump and probe beam were set to 800

and 200 nm, respectively. The repetition rate was set to 1000 kHz using a pulse picker. The energy and angular resolutions were set to be 8 meV and 0.1° , respectively. The Fermi level (E_F) of the sample was calibrated with a gold film deposited onto the substrate. To avoid contamination of the sample surface in ex situ ARPES measurements, we covered the film with amorphous Se immediately after the epitaxy, transferred it to a separate ARPES chamber, and then decapped the amorphous Se film by heating under UHV.

STM measurements were carried out using a custom-made ultrahigh vacuum STM system⁵⁷. Se capping layers for surface protection of TaSe₂ films were removed in the STM chamber by Ar⁺ ion sputtering for 30 min and annealing at 200 °C for 60 min. STM measurements were performed with PtIr tips at 4.8 K under UHV below 2.0×10^{-10} Torr. All STM images were obtained in constant-current mode.

Data availability

The data that support the findings of this study are available from the corresponding author upon reasonable request.

Received: 23 January 2021; Accepted: 17 September 2021;

Published online: 07 October 2021

References

- Mott, N. F. & Peierls, R. Discussion of the paper by de Boer and Verwey. *Proc. Phys. Soc. Lond., Ser. A* **49**, 72–73 (1937).
- Imada, M., Fujimori, A. & Tokura, Y. Metal-insulator transitions. *Rev. Mod. Phys.* **70**, 1039–1263 (1998).
- Balents, L. Spin liquids in frustrated magnets. *Nature* **464**, 199–208 (2010).
- Law, K. T. & Lee, P. A. 1T-TaS₂ as a quantum spin liquid. *Proc. Natl Acad. Sci. USA* **114**, 6996–7000 (2017).
- Dagotto, E. Correlated electrons in high-temperature superconductors. *Rev. Mod. Phys.* **66**, 763–840 (1994).
- Lee, P. A., Nagaosa, N. & Wen, X.-G. Doping a Mott insulator: physics of high-temperature superconductivity. *Rev. Mod. Phys.* **78**, 17–85 (2006).
- Yang, S.-L. et al. Revealing the Coulomb interaction strength in a cuprate superconductor. *Phys. Rev. B* **96**, 245112 (2017).
- Xie, B. P. et al. High-energy scale revival and giant kink in the dispersion of a cuprate superconductor. *Phys. Rev. Lett.* **98**, 147001 (2007).
- Ohta, Y., Yohyama, T. & Maekawa, S. Charge-transfer gap and superexchange interaction in insulating cuprates. *Phys. Rev. Lett.* **66**, 1228 (1995).
- Cao, Y. et al. Unconventional superconductivity in magic-angle graphene superlattices. *Nature* **556**, 43–50 (2018).
- Cao, Y. et al. Correlated insulator behaviour at half-filling in magic-angle graphene superlattices. *Nature* **556**, 80–84 (2018).
- Fazekas, P. & Tosatti, E. Electrical, structural and magnetic properties of pure and doped 1T-TaS₂. *Philos. Mag. B* **39**, 229–244 (1979).
- Fazekas, P. & Tosatti, E. Charge carrier localization in pure and doped 1T-TaS₂. *Phys. B* **99**, 183–187 (1980).
- Smith, N. V., Kevan, S. D. & DiSalvo, F. J. Band structures of the layer compounds 1T-TaS₂ and 2H-TaSe₂ in the presence of commensurate charge-density waves. *J. Phys. C Solid State Phys.* **18**, 3175–3189 (1985).
- Rosnagel, K. & Smith, N. V. Spin-orbit coupling in the band structure of reconstructed 1T-TaS₂. *Phys. Rev. B* **73**, 073106 (2006).
- Freericks, J. K., Krishnamurthy, H. R., Ge, Y., Liu, A. Y. & Pruschke, T. Theoretical description of time-resolved pump/probe photoemission in TaS₂: a single-band DFT+DMFT(NRG) study within the quasiequilibrium approximation. *Phys. Status Solid B* **246**, 948–954 (2009).
- Klanjsek, M. et al. A high-temperature quantum spin liquid with polaron spins. *Nat. Phys.* **13**, 1130–1136 (2017).
- Nakata, Y. et al. Selective fabrication of Mott-insulating and metallic monolayer TaSe₂. *ACS Appl. Nano Mater.* **1**, 1456–1460 (2018).
- Nakata, Y. et al. Monolayer 1T-NbSe₂ as a Mott insulator. *NPG Asia Mater.* **8**, e321 (2016).
- Chen, Y. et al. Strong correlations and orbital texture in single-layer 1T-TaSe₂. *Nat. Phys.* **16**, 218–224 (2020).
- Bovet, M. et al. Pseudogapped Fermi surfaces of 1T-TaS₂ and 1T-TaSe₂: a charge density wave effect. *Phys. Rev. B* **69**, 125117 (2004).
- Stoltz, D., Biemann, M., Bovet, M., Schlapbach, L. & Berger, H. Tunneling evidence for spatial location of the charge-density-wave induced band splitting in 1T-TaSe₂. *Phys. Rev. B* **76**, 073410 (2007).
- Qiao, S. et al. Mottness collapse in 1T-TaS_{2-x}Se_x transition-metal dichalcogenide: an interplay between localized and itinerant orbitals. *Phys. Rev. X* **7**, 041054 (2017).
- Butler, C. J., Yoshida, M., Hanaguri, T. & Iwasa, Y. Mottness versus unit-cell doubling as the driver of the insulating state in 1T-TaS₂. *Nat. Commun.* **11**, 2477 (2020).
- Hughes, H. P. & Scarfe, J. A. Site specific photohole screening in a charge density wave. *Phys. Rev. Lett.* **74**, 3069–3072 (1995).
- Horiba, K. et al. Angle-resolved photoemission study in the commensurate CDW phase of 1T-TaSe₂. *Phys. B* **284–288**, 1665–1666 (2000).
- Perfetti, L. et al. Spectroscopic signatures of a bandwidth-controlled Mott transition at the surface of 1T-TaSe₂. *Phys. Rev. Lett.* **90**, 166401 (2003).
- Chen, P. et al. Charge density wave transition in single-layer titanium diselenide. *Nat. Commun.* **6**, 8943 (2015).
- Colonna, S. et al. Mott phase at the surface of 1T-TaSe₂ observed by scanning tunneling microscopy. *Phys. Rev. B* **94**, 036405 (2005).
- Chen, P. et al. Hidden order and dimensional crossover of the charge density waves in TiSe₂. *Sci. Rep.* **6**, 37910 (2016).
- Perfetti, L. et al. Femtosecond dynamics of electronic states in the Mott insulator 1T-TaS₂ by time resolved photoelectron spectroscopy. *New J. Phys.* **10**, 053019 (2008).
- Perfetti, L. et al. Time evolution of the electronic structure of 1T-TaS₂ through the insulator-metal transition. *Phys. Rev. Lett.* **97**, 067402 (2006).
- Sohrt, C., Stange, A., Bauer, M. & Rosnagel, K. How fast can a Peierls–Mott insulator be melted? *Faraday Discuss* **171**, 243–257 (2014).
- Vaskivskiy, I. et al. Controlling the metal-to-insulator relaxation of the metastable hidden quantum state in 1T-TaS₂. *Sci. Adv.* **1**, e1500168 (2015).
- Shi, X. et al. Ultrafast electron calorimetry uncovers a new long-lived metastable state in 1T-TaSe₂ mediated by mode-selective electron-phonon coupling. *Sci. Adv.* **5**, eaav4449 (2019).
- Zhang, Y. et al. Coherent modulation of the electron temperature and electron-phonon couplings in a 2D material. *Proc. Natl Acad. Sci. USA* **117**, 8788 (2020).
- Kolekar, S. et al. Controlling the charge density wave transition in monolayer TiSe₂: substrate and doping effects. *Adv. Quantum Technol.* **1**, 1800070 (2020).
- Cai, P. et al. Visualizing the evolution from the Mott insulator to a charge-ordered insulator in lightly doped cuprates. *Nat. Phys.* **12**, 1047 (2016).
- Xu, P. et al. Superconducting phase in the layered dichalcogenide 1T-TaS₂ upon inhibition of the metal-insulator transition. *Phys. Rev. B* **81**, 172503 (2010).
- Li, L. J. et al. Fe-doping-induced superconductivity in the charge-density-wave system 1T-TaS₂. *Europhys. Lett.* **97**, 67005 (2012).
- Ang, R. et al. Real-space coexistence of the melted Mott state and superconductivity in Fe-substituted 1T-TaS₂. *Phys. Rev. Lett.* **109**, 176403 (2012).
- Yu, Y. et al. Gate-tunable phase transitions in thin flakes of 1T-TaS₂. *Nat. Nanotech.* **10**, 270–276 (2015).
- Wilson, J. A., Di Salvo, F. J. & Mahajan, S. Charge-density waves in metallic, layered, transition-metal dichalcogenides. *Phys. Rev. Lett.* **32**, 882–885 (1974).
- Rosnagel, K. On the origin of charge-density waves in select layered transition-metal dichalcogenides. *J. Phys. Condens. Matter* **23**, 213001 (2011).
- Calandra, M. Phonon-assisted magnetic Mott-insulating state in the charge density wave phase of single-layer 1T-NbSe₂. *Phys. Rev. Lett.* **121**, 026401 (2018).
- Aryanpour, K., Pickett, W. E. & Scalettar, R. T. Dynamical mean-field study of the Mott transition in the half-filled Hubbard model on a triangular lattice. *Phys. Rev. Lett.* **74**, 085117 (2006).
- Werner, P., Sakuma, R., Nilsson, F. & Aryasetiawan, F. Dynamical screening in La₂CuO₄. *Phys. Rev. B* **91**, 125142 (2015).
- Kamil, E. et al. Electronic structure of single layer 1T-NbSe₂: interplay of lattice distortions, non-local exchange, and Mott–Hubbard correlations. *J. Phys. Condens. Matter* **30**, 325601 (2018).
- Liu, L. et al. Direct identification of Mott Hubbard band pattern beyond charge density wave superlattice in monolayer 1T-NbSe₂. *Nat. Commun.* **12**, 1978 (2021).
- Zhang, K., Si, Chen, Lian, C. S., Zhou, J. & Sun, Z. Mottness collapse in monolayer 1T-TaSe₂ with persisting charge density wave order. *J. Mater. Chem. C* **8**, 9742–9747 (2020).
- Ritschel, T. et al. Orbital textures and charge density waves in transition metal dichalcogenides. *Nat. Phys.* **11**, 328–331 (2015).
- Yan, J.-A., Cruz, M. A. D., Cook, B. & Varga, K. Structural, electronic and vibrational properties of few-layer 2H- and 1T-TaSe₂. *Sci. Rep.* **5**, 16646 (2015).
- Nakata, Y. et al. Anisotropic band splitting in monolayer NbSe₂: implications for superconductivity and charge density wave. *npj 2D Mater. Appl.* **2**, 12 (2018).
- Umamoto, Y. et al. Pseudogap, Fermi arc, and Peierls-insulating phase induced by 3D–2D crossover in monolayer VSe₂. *Nano Res.* **12**, 165 (2019).
- Sugawara, K. et al. Monolayer VTe₂: incommensurate Fermi surface nesting and suppression of charge density waves. *Phys. Rev. B* **99**, 241404(R) (2019).

56. Zhang, H. et al. Self-energy dynamics and mode-specific phonon threshold effect in a Kekulé-ordered graphene. <https://arxiv.org/abs/2106.01358> (2021).
57. Iwaya, K. et al. Atomic-scale visualization of oxide thin-film surfaces. *Sci. Technol. Adv. Mater.* **19**, 282 (2018).

Acknowledgements

We thank Takumi Sato, T. Taguchi, and C.-W. Chuang for their assistance in the ARPES measurements. We also thank NSRRC-TLS for access to beamline BL21B1. This work was supported by JST-CREST (no. JPMJCR18T1), JST-PRESTO (no. JPMJPR20A8), Grant-in-Aid for Scientific Research on Innovative Areas “Topological Materials Science” (JSPS KAKENHI Grant numbers JP15H05853 and JP15K21717), Grant-in-Aid for Scientific Research (JSPS KAKENHI Grant numbers JP21H04435, JP17H01139), National Natural Science Foundation of China (11725418, 11427903), Ministry of Science and Technology of China (2016YFA0301004, 2015CB921001), Beijing Advanced Innovation Center for Future Chip (ICFC), Tsinghua University Initiative Scientific Research Program, Tohoku-Tsinghua Collaborative Research Fund, Grant for Basic Science Research Projects from the Sumitomo Foundation, Research Foundation of the Electrotechnology of Chubu, Ministry of Science and Technology of the Republic of China, Taiwan, under contract no. MOST 108-2112-M-213-001-MY3, and World Premier International Research Center, Advanced Institute for Materials Research. Y. N. and T. K. acknowledge support from GP-Spin at Tohoku University. A.C. and C.M.C. thank the Ministry of Science and Technology (MOST) of Taiwan, Republic of China, for financially supporting this research under Contract No. MOST 109-2911-I-213-501.

Author contributions

The work was planned and proceeded by discussion among Y.N., K.S. and T.S. Y.N. and K.S. fabricated ultrathin films. Y.N., K.S., A.C., C.B., S.Z., P.C., C.C., T.K., Y.S. and S.Z. performed the ARPES measurements. H.O. and T.F. performed the STM measurements. Y.N., A.C., T.T. and T.S. finalized the paper with inputs from all the authors.

Competing interests

The authors declare no competing interests.

Additional information

Supplementary information The online version contains supplementary material available at <https://doi.org/10.1038/s41467-021-26105-1>.

Correspondence and requests for materials should be addressed to Takafumi Sato.

Peer review information *Nature Communications* thanks the anonymous reviewers for their contribution to the peer review of this work. Peer reviewer reports are available.

Reprints and permission information is available at <http://www.nature.com/reprints>

Publisher's note Springer Nature remains neutral with regard to jurisdictional claims in published maps and institutional affiliations.



Open Access This article is licensed under a Creative Commons Attribution 4.0 International License, which permits use, sharing, adaptation, distribution and reproduction in any medium or format, as long as you give appropriate credit to the original author(s) and the source, provide a link to the Creative Commons license, and indicate if changes were made. The images or other third party material in this article are included in the article's Creative Commons license, unless indicated otherwise in a credit line to the material. If material is not included in the article's Creative Commons license and your intended use is not permitted by statutory regulation or exceeds the permitted use, you will need to obtain permission directly from the copyright holder. To view a copy of this license, visit <http://creativecommons.org/licenses/by/4.0/>.

© The Author(s) 2021